

Semantic segmentation of multispectral photoacoustic images using deep learning

Janeke Gröhl^{1,†,‡}, Melanie Schellenberg^{1,†,*}, Kris Dreher^{1,2}, Niklas Holzwarth¹, Minu D. Tizabi¹, Alexander Seitel¹, and Lena Maier-Hein^{1,3,4,*}

¹German Cancer Research Center, Computer Assisted Medical Interventions, Heidelberg, Germany;

²Heidelberg University, Faculty of Physics and Astronomy, Heidelberg, Germany;

³Heidelberg University, Medical Faculty, Heidelberg, Germany;

⁴Heidelberg University, Faculty of Mathematics and Computer Science, Heidelberg, Germany

† These authors contributed equally.

‡ Now at Cancer Research UK Cambridge Institute, University of Cambridge, Robinson Way, Cambridge, CB2 0RE, U.K.

* Send correspondence to melanie.schellenberg@dkfz-heidelberg.de or l.maier-hein@dkfz-heidelberg.de

Photoacoustic imaging has the potential to revolutionise healthcare due to the valuable information on tissue physiology that is contained in multispectral photoacoustic measurements. Clinical translation of the technology requires conversion of the high-dimensional acquired data into clinically relevant and interpretable information. In this work, we present a deep learning-based approach to semantic segmentation of multispectral photoacoustic images to facilitate the interpretability of recorded images. Manually annotated multispectral photoacoustic imaging data are used as gold standard reference annotations and enable the training of a deep learning-based segmentation algorithm in a supervised manner. Based on a validation study with experimentally acquired data of healthy human volunteers, we show that automatic tissue segmentation can be used to create powerful analyses and visualisations of multispectral photoacoustic images. Due to the intuitive representation of high-dimensional information, such a processing algorithm could be a valuable means to facilitate the clinical translation of photoacoustic imaging.

Keywords:

Medical Image Segmentation, Deep Learning, Multispectral Imaging, Photoacoustics

1. Introduction

Photoacoustic imaging (PAI) is an emerging and rapidly developing imaging modality that enables real-time, non-invasive, and radiation-free measurement of optical tissue properties¹. PAI has the potential to spatially resolve valuable morphological and functional tissue information, such as the oxygenation saturation (sO_2)², up to several centimetres in depth³. While theoretically, PAI is capable of measuring such parameters, the technique is heavily limited by non-linear fluence effects⁴, which lead to a colouring of the underlying absorption spectra⁵, thus introducing errors in the derived functional parameter values. Therefore, the recovery of accurate and reliable parameters from photoacoustic (PA) measurements is an ongoing field of research^{6,7}. At the same time, the provision of accurate and interpretable visualisations of multispectral PA measurement data is a crucial step to be taken towards the clinical translation of PAI. One way to achieve this could be to automatically classify distinct tissue classes based on the multispectral PA signal, segmenting the tissue into disjunct regions which can be annotated with relevant information, such as structure-specific sO_2 . A promising use of this would be the creation of a high-level and intuitive visualisation of the measurement data, as illustrated in Fig. 1.

Several groups have already worked on methods for automatic segmentation of regions of interest, for example for the automatic identification of structures in mouse images⁸ or for vessel segmentation both in simulation studies⁹ and experimental settings^{10,11}. Furthermore, work has been conducted towards the annotation of different skin layers in raster-scanned images¹². However, to our knowledge, no work has been published to date on the automatic *multi-label* semantic annotation of multispectral PA images in humans.

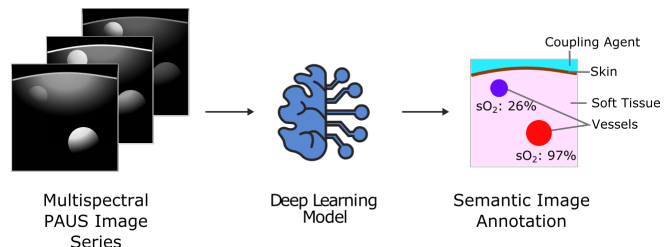


Fig. 1. Overview of the proposed approach to automatic semantic image annotation. A deep learning network automatically estimates annotations based on photoacoustic (PA), ultrasound (US), and a combination of both (PAUS) images.

In this paper, we present a deep learning-based method to automatically create *multi-label* semantic tissue annotations of multispectral PA images. In a first feasibility study, the proposed algorithm was trained on a set of manually annotated forearm, calf, and neck measurements in a supervised manner. Since many commonly used PA devices capture PA and ultrasound (US) data simultaneously^{13,14}, we compared the performance of our method for different types of input images, namely (1) PA images, (2) US images and (3) combined PA and US images which we refer to a PAUS images.

2. Materials and methods

In this section, we describe the deep learning-based method for semantic annotation of PA data (Sec. A), the data set we acquired for training and validating our method (Sec. B) as well as our experimental design (Sec. C).

A. Segmentation method. Due to its breakthrough successes in various fields of research and practice, we based our segmentation method on deep learning. In this context, we investigated two well-known neural network architectures with complementary strengths:

Choice of architectures. In a recent literature review¹⁵, we found the U-Net¹⁶ to be the by far most commonly used and most successful network architecture for deep learning applications in PAI. Compared to previous architectures used for image segmentation, it requires fewer training images, yields more precise segmentations, and is thus particularly well-suited for medical applications. Another popular network design is the fully-connected feed-forward neural network (FCNN). In the context of PA, FCNN are well-suited for working with single-pixel spectra as input, which increases the effective number of training samples and makes it easy to work with sparsely annotated data.

Implementation details of the U-Net. The U-Net was implemented based on the original U-Net design¹⁶. Leaky rectified linear units (ReLUs) were used in between each convolutional layer. The model uses 2×2 max pooling for downscaling, 2×2 transpose convolutions for upscaling, and all convolution layers have a kernel size of 3×3 and padding of 1×1 , followed by a leaky ReLU. For higher robustness against overfitting, we added dropout layers with a dropout rate of 25% to each convolutional layer of the network. The number of input channels and output channels was determined by N_{in} and N_{out} as defined in the FCNN section. For training of the U-Net, we used a combination of the Cross-Entropy Loss¹⁷ and the Soft Dice Loss, as proposed by Jadon et al.¹⁸. We implemented the training in Pytorch¹⁷ and the details on the training hyperparameters that were chosen according to a grid search for both networks are listed in Table 1.

Hyperparameter	U-Net	FCNN
Learning rate	$1e^{-3}$	$1e^{-4}$
Batch size	25	$1e^{-4}$
Batches per epoch	11	1000
Number of epochs	1000	200

Table 1. Overview of our hyperparameter choices for the two network architectures for the U-Net and the fully-connected neural network (FCNN).

Implementation details of the FCNN. The FCNN consisted out of an input layer of size N_{in} , four hidden layers of size $2 * N_{in}$ and an output layer of size $N_{out} = 7$. N_{in} was chosen corresponding to the number of input channels (i.e. 26 for PA and 27 for PAUS). Dropout layers (p=0.2) and leaky ReLUs were used in between each fully connected layer. A diagram of the network architecture can be found in a previous publication¹⁹. For training of the FCNN, we used a Soft Margin Loss¹⁷.

Data Augmentation. We did not use noise augmentation because initial results on the validation set yielded no significant differences in segmentation performance. Instead, we used flipping, shearing, and rotation operations to slightly change the morphology of the images. The shearing and rotation angles were randomly chosen between -5° and 5° and flipping was done along the x-axis. Because single-pixel spectra are not affected by these morphological operations, we were not able to apply this augmentation strategy to the training of the FCNN.

B. Data acquisition and annotation. The dataset consists of multispectral PA images of ten human healthy volunteers. The experiments were carried out in accordance with relevant guidelines and regulations and informed consent was obtained from all subjects. They were approved by the ethics committee of the medical faculty of Heidelberg University under reference number S-451/2020 and the study is registered with the German Clinical Trials Register under reference number DRKS00023205. For each of the ten volunteers, the neck, calf, and forearm were imaged at three distinct locations both on the left and right side of the body, yielding $N = 180$ unique multispectral PA and US image pairs in total.

The images were acquired using the MSOT Acuity Echo device (iThera Medical, Munich, Germany) using 26 wavelengths equidistant from 700 nm to 950 nm. Each distinct location was imaged for approximately 30 seconds. The US images were reconstructed using a proprietary backprojection algorithm and the PAI images were reconstructed using an in-house developed Delay-And-Sum

(DAS) algorithm²⁰ within the Medical Imaging Interaction Toolkit (MITK)²¹. The sequences were post-processed including a correction for variations in the laser pulse energy and optimization of the Signal-to-Noise-Ratio (SNR). To correct for the variations in laser pulse energy, the PA images were divided by the respective laser pulse energies. As a consequence of the different reconstruction algorithms with different fields of view used for PAI and US images, the PAI images were cropped to enable a co-registration with the US images. To optimise the SNR, the co-registered sequences were divided into four sections of approximately 8 seconds. These sections were averaged and the one with the highest acutance was used, which is defined by the mean of the image gradients.

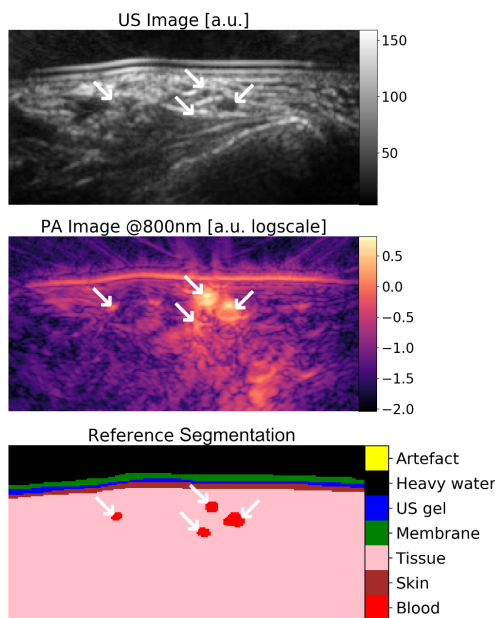


Fig. 2. Example of the forearm data set. (Top) An ultrasound (US) image, (center) a photoacoustic (PA) image at 800 nm, and (bottom) the reference segmentation mask. The white arrows denote the blood vessels in the US, PA, and segmentation image.

After image reconstruction and post-processing, the images were manually annotated by three annotators using a standardised annotation protocol (cf. Appendix A). Seven annotation classes were distinguished during the annotation process: blood, skin, US gel, transducer membrane, coupling agent in the transducer head (mostly heavy water), other tissue, and coupling artefact. The "other tissue" category was assigned to the tissue below the skin layer that does not fall into the blood category and comprises e.g. muscle tissue, fat tissue, conjunctive tissue, etc. The coupling artefact class was introduced to account for a loss of signal at the edges of the image due to a lack of coupling of the transducer to the skin. Fig. 2 shows an example set of an US image, a PA image at 800 nm, and the corresponding segmentation mask of one of the forearm images. As

accurate labels are key in supervised machine learning, we ensured the plausibility of the segmentations by comparing the averaged normalised spectra of several structures (skin, a highly oxygenated vessel, and a vessel with low oxygenation) to respective values from the literature²² (i.e., the absorption spectra of melanin, deoxyhemoglobin, and oxyhemoglobin), as shown in Fig. 3.

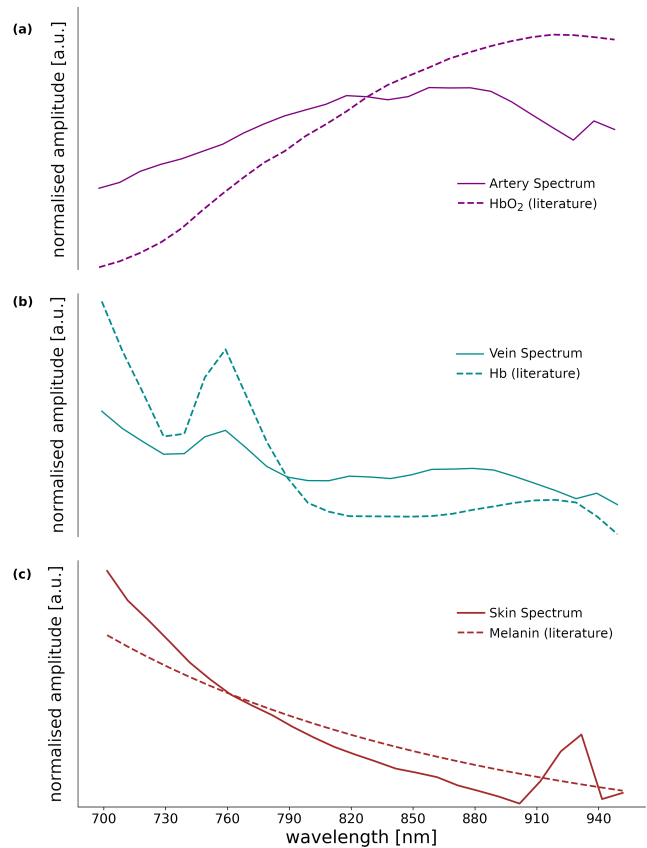


Fig. 3. Comparison of (a) arterial blood, (b) venous blood, and (c) skin spectra of one measured example image with the respective literature spectra. The corresponding pixels per segmentation class were extracted from an arbitrarily chosen reference segmentation and we additionally differentiated between venous and arterial blood for the purpose of this comparison. The spectra were averaged per segmentation class and normalised and the literature spectra were normalised, too. Despite non-linear influence of the light fluence, the bandwidth limitations of the detection elements and the influence of noise, the spectra are in good agreement. Specifically, one can see a monotonous decrease of the signal, where melanin is the dominant chromophore, as well as the characteristic wavelength-dependent behaviour where blood is dominant.

The data was divided into three sets: A training set that comprised 138 images of 8 volunteers, a validation set that comprised 6 images, and a test set that comprised 36 images of 2 volunteers, maximising the number of training data while retaining a small validation data set for hyperparameter tuning and ensuring a sizable test data set containing previously completely unseen images²³.

C. Experimental Design. The primary goal of the experiments was to investigate the general feasibility of the proposed deep learning-based approach for multi-label semantic image annotation. To this end, we conducted two experiments:

We first performed a **feasibility experiment**, in which we used different combinations of data and inference models to evaluate differences in performance when segmenting the labelled tissue classes. We trained the FCNN and U-Net architectures using only the US and PA data and a combination of both, PA and US data (PAUS). It has to be noted that we trained only the U-Net with US data as sole input because it would not make sense to apply the FCNN to one-dimensional input data. We systematically compared the performances of these algorithm/data combinations using the Dice score²⁴ and the True Positive Rate (TPR)²⁵, which we calculated for each of the target labels.

To investigate the **robustness** of the proposed approach with respect to morphologically different target structures, we conducted an experiment, in which we used different target structures for training and testing our algorithm. Specifically, we trained the networks exclusively on the forearm and calf measurements of the training set and estimated the tissue classes on the neck measurements of the test set. The different combinations of data and inference models were analogous to the feasibility experiments.

3. Results

The following paragraphs detail the qualitative and quantitative results of the investigated deep learning-based methods for multi-label semantic image annotation.

A. Feasibility experiment. Table 2 shows the Dice score and TPR results of all input data for the U-Net and FCNN segmentation architectures. Fig. 4 presents the distribution of Dice scores for all tissue classes (after calculating the mean of the Dice values for all structures in each image), blood, and for skin. The model performances differed the most in case of blood segmentation. Especially for this tissue class, the U-Net model architecture performed substantially better than the FCNN model in this first feasibility experiment. The results further indicate that it is beneficial to use PA or PAUS data compared to using US data as sole input. In this first experiment with only two test patients, we did not observe any substantial differences between volunteers, body sides, or target structure sites.

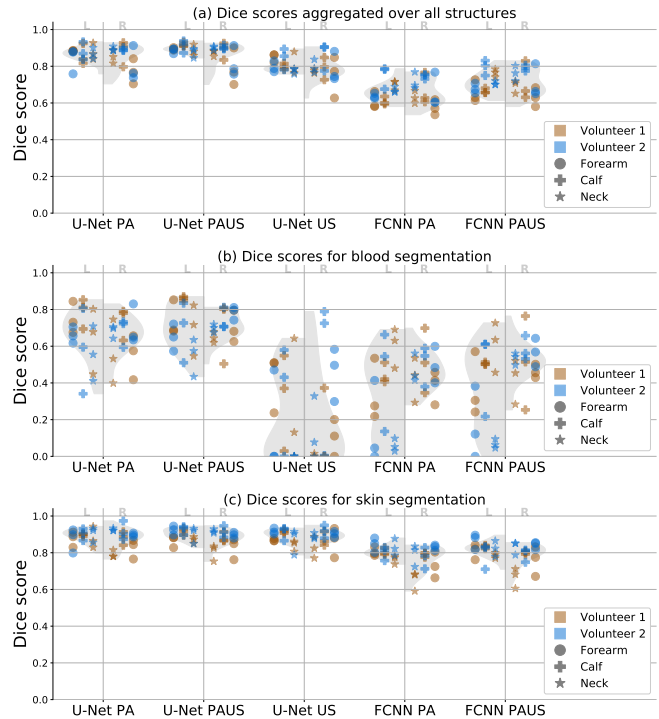


Fig. 4. Dice scores achieved in the feasibility experiment (a) averaged over all structures, (b) for the blood, and (c) for the skin. A separate plot is shown for each of the algorithm/data combinations. Colour/Shape coding enables distinguishing the two volunteers (blue vs brown) as well as the different target structures (the three shapes). Measurements from the left and right side of the volunteers bodies are plotted at the left and right of the vertical lines, respectively. The grey density plots show the relative score frequencies separately for each side.

	Tissue Class	U-Net PA	U-Net PAUS	U-Net US	FCNN PA	FCNN PAUS
Dice score	Blood	0.66	0.70	0.23	0.40	0.44
	Skin	0.88	0.89	0.88	0.78	0.80
	Tissue	0.98	0.98	0.98	0.88	0.90
	Membrane	0.91	0.92	0.92	0.76	0.83
	US gel	0.85	0.87	0.87	0.72	0.78
	Heavy water	0.99	0.99	0.99	0.61	0.72
	Artefact	0.48	0.59	0.59	0.05	0.07
TPR	Blood	0.68	0.74	0.20	0.35	0.39
	Skin	0.92	0.93	0.92	0.79	0.83
	Tissue	0.99	0.98	0.99	0.96	0.96
	Membrane	0.92	0.94	0.94	0.75	0.84
	US gel	0.84	0.86	0.85	0.68	0.72
	Heavy water	0.99	0.99	0.99	0.50	0.64
	Artefact	0.41	0.53	0.52	0.02	0.04

Table 2. Dice scores and True Positive Rates (TPRs) achieved with the feasibility experiments for the U-Net and fully-connected neural network (FCNN) architectures. For each of the tissue classes, the Dice score and TPR were calculated separately for all input data.

Fig. 5 shows the result plots for the image corresponding to the median Dice score for the blood class. While the FCNN estimations for the PA data sets qualitatively look plausible as well, there is much more noise in the estimated labels compared to the U-Net estimates.

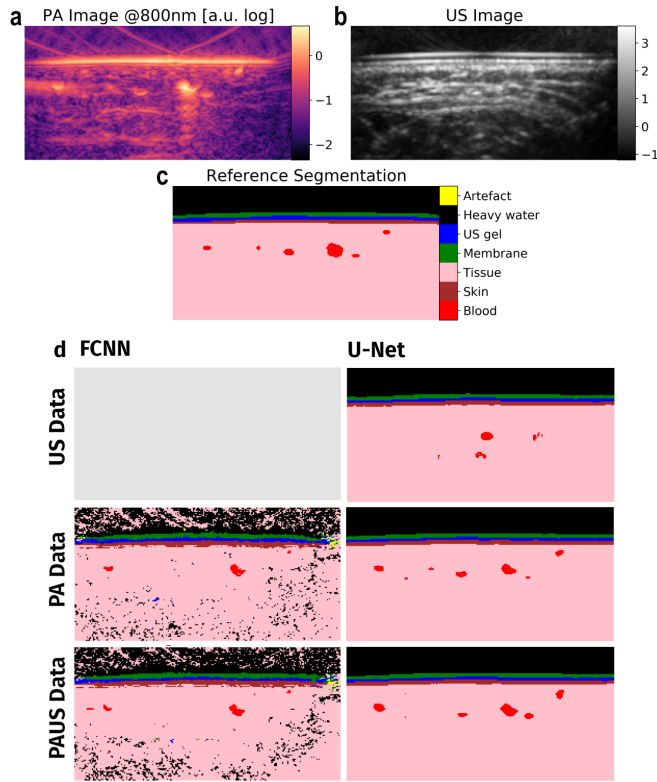


Fig. 5. Overview of the estimation results for the different data/architecture combinations. The image was chosen according to the median blood Dice score for the U-Net using photoacoustic and ultrasound (PAUS) as input. **a** Logscaled photoacoustic (PA) image at 800 nm, **b** Ultrasound (US) image, and **c** reference segmentations of the chosen image. The predicted segmentation maps **d** for the fully-connected neural network (FCNN) and the U-Net based on US input data, PA input data, and PAUS input data. Note, the FCNN is not trained on US data only due to the one-dimensional nature of the data.

The segmentation of blood vessels can be considered one of the most crucial tasks for segmentation algorithms in the field of photoacoustics¹⁵. The U-Nets with PA and PAUS input data performed well in this regard. Fig. 6 shows the segmentation results for the cases where the best / median / and worst Dice scores for the blood class were achieved by the U-Net on the PAUS data set. Usually, all major vessel structures were successfully segmented. Nevertheless, especially the image corresponding to the worst Dice score highlights the variances in shape and size of the estimated vessel structures compared to the reference annotations.

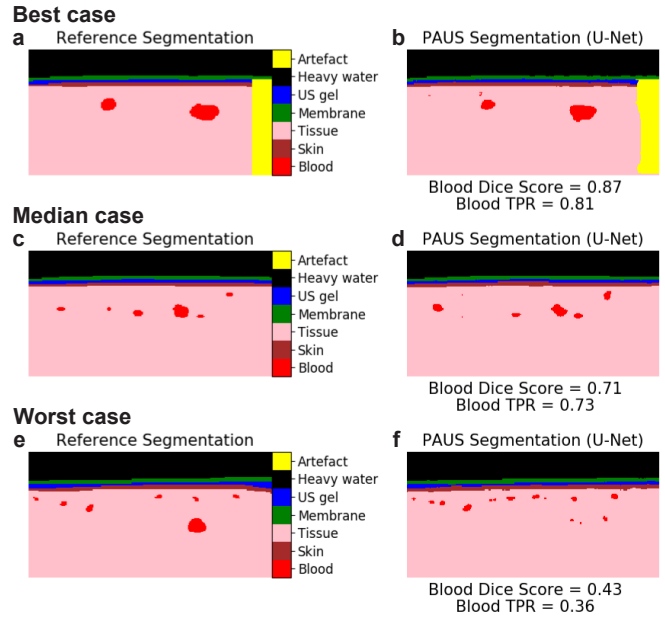


Fig. 6. The best, median, and worst U-Net estimates of the feasibility experiments on photoacoustic and ultrasound (PAUS) data with respect to the blood Dice score. **a-c** Reference segmentations and **d-f** predicted U-Net PAUS segmentations with **a,d** best, **b,e** median, and **c,f** worst Dice scores. The Dice scores and True Positive Rates (TPRs) are shown respectively.

B. Robustness experiment. The Dice scores and TPRs for training on the forearm and calf data sets and testing on the neck data sets only are shown in Table 3. Fig. 7 shows the distribution of Dice scores of the mean of all tissue classes, of blood segmentation, and of skin segmentation with respect to the test volunteer, the segmented tissue type, and the measurement site. On average, the Dice score decreased by 21.2 %, 2.3 %, and 4.2 % for the U-Net and 2.5 %, 5.1 %, and 5.1 % for the FCNN for blood, skin, and all tissue classes, respectively when trained on PA data. A similar performance was observed for PAUS data.

The models performed worse for blood than for most other structures and the U-Net yielded better results than the FCNN model when including multispectral data, i.e., when complementing the US information with PA input data (PAUS).

	Tissue Class	U-Net PA	U-Net PAUS	U-Net US	FCNN PA	FCNN PAUS
Dice score	Blood	0.49	0.63	0.00	0.39	0.35
	Skin	0.86	0.88	0.85	0.74	0.74
	Tissue	0.99	0.99	0.98	0.89	0.90
	Membrane	0.88	0.91	0.92	0.78	0.85
	US gel	0.83	0.85	0.85	0.65	0.72
	Heavy water	0.99	0.99	0.99	0.52	0.62
	Artefact	N/A	N/A	N/A	N/A	N/A
TPR	Blood	0.60	0.69	0.00	0.48	0.48
	Skin	0.89	0.88	0.84	0.70	0.68
	Tissue	0.98	0.98	0.98	0.97	0.96
	Membrane	0.89	0.93	0.94	0.74	0.85
	US gel	0.82	0.83	0.83	0.55	0.60
	Heavy water	0.99	0.99	0.99	0.38	0.50
	Artefact	N/A	N/A	N/A	N/A	N/A

Table 3. Dice scores and True Positive Rates (TPRs) achieved with the robustness experiments, where forearm and calf data of training data set were used for training and neck data of test data set was used for testing. For each of the tissue classes, the Dice score and TPR were calculated separately for each data/architecture combination.

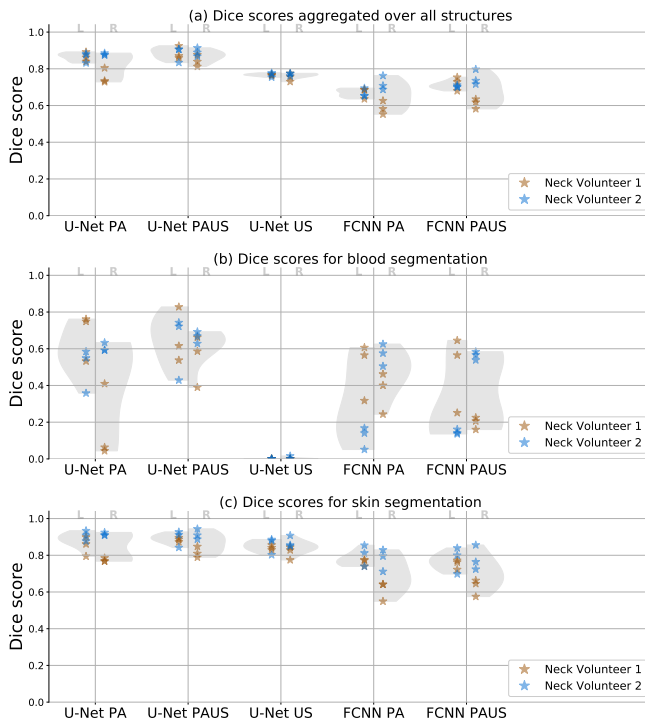


Fig. 7. Dice scores of neck data achieved in the robustness experiment (a) aggregated over all structures, (b) for the blood, and (c) for the skin. A separate plot is shown for each of the algorithm/data combinations. Colour/Shape coding enables distinguishing the two volunteers (blue vs brown). Measurements from the left and right side of the volunteers bodies are plotted at the left and right of the vertical lines, respectively. The grey density plots show the relative score frequencies separately for each side.

4. Discussion

To our knowledge, this paper is the first to show that fully-automatic *multi-label* semantic image annotation of PA images with deep learning is feasible. To achieve this, we used two neural network architectures, an FCNN that utilises single pixel spectral information and a U-Net that incorporates spatial context information. While the U-Net performed better throughout the experiments, initial results suggest that the FCNN could be more robust when applied to previously unseen body regions.

In our feasibility experiment, the U-Net achieved consistently better results compared to the FCNN. We attribute this to its ability to account for the spatial image context. However, even though the FCNN was only able to estimate the labels based on single-pixel spectra, the resulting images were plausible as well. The overall results of the networks were very convincing, achieving high Dice scores for the majority of classes. The worst performances were achieved for the blood and coupling artefact classes, for which the most obvious explanation is the difficulty of annotating these areas. Nevertheless, the spectra of the tissue classes seem to be very characteristic for the respective class. The images showing the worst Dice score results revealed that there are two sorts of edge cases that are not well handled by the trained network: on the one hand, big or deep vessels were generally under-segmented by the algorithm, possibly caused by the exponential loss of signal in greater depths, and shallow small superficial vessels were sometimes over-segmented; also, signal patches not identified as vessels by the annotators were sometimes annotated as vessels by the algorithm.

In our robustness experiment, the performance of the U-Net decreased for blood in comparison to the feasibility experiment. One reason could be the domain shift between different body regions that was explicitly included in this experiment. This indicates that the geometrical variations between different body regions might have an impact on the algorithm performance although the tissue composition of the regions investigated was relatively similar. It can be expected that the performance would degrade even further for vastly different structures (e.g. in abdominal surgery). It has to be noted that the test data set of the robustness experiment compared to the feasibility experiment was decreased in size by a factor of three, which may also cause the decrease in performance. The experimental results could be a further indicator of the high potential of FCNNs for robust interpretation of single-pixel multispectral imaging data. Compared to convolutional approaches, they are by design more independent of morphological variations within the

training and target domains.

In the broader context of biomedical image analysis, several studies²⁶ suggest that the model performance can be impeded by the quality of the reference segmentation labels. The main problem with manual labelling is that the process is time-consuming, requires expert knowledge, and is error-prone. Although we put a lot of effort in generating a structured annotation protocol for standardised annotation and the segmentation masks were reviewed by at least one other person, many ambiguities remained. These were mostly caused by the imaging process, as the apparent sizes of structures might not reflect their real size. For example, in some images, we have found size and position mismatches between the PA and US images, which might be introduced by differences in the speed of sound across different volunteers. Further sources for ambiguity in the signal were a blurring of the PA signals, which can be attributed to the limited bandwidth of the US detection elements, their impulse response, as well as artefacts introduced by the reconstruction algorithm. These inherent ambiguities might be resolvable by multi-modal image registration²⁷ or by capturing 3D instead of 2D images to exploit the spatial context information. However, obtaining high-quality 3D reconstructions with handheld linear transducers is usually very time-consuming and requires the use of additional hardware²⁸. Furthermore, we introduced the coupling artefact tissue class in order to label areas where there was no direct contact between the probe and the tissue. However, these varied in appearance and were sometimes difficult to discern from valid images, leading to further ambiguities.

While our first study indicates that *multi-label* semantic annotation of PA and/or US images with deep learning is feasible, our initial results should be interpreted with care. The biggest limitation of our study is the fact that we had a very low number of test images. With only 36 images from 2 volunteers, no broad conclusions should be drawn from the results, especially with respect to the relative performance of the different architecture/input combinations. A related potential problem is the hierarchical nature of the data set (10 volunteers, three imaging sites, three images per site, left and right side of the body), which complicates a rigorous statistical analysis. In fact, based on the data visualisation in Fig. 4, we found no clear evidence that the algorithms performed differently on test images of the left and right side of the body. At the same time, in some cases there is a clustering of Dice score results within the same site. Our test data therefore cannot be regarded as independent and this was the reason for us to report the mean performance without standard deviation in Tables 2 and 3.

Additionally, our experimental design may have led to a bias favoring networks trained on PAUS data. On the one hand, the manual annotations were done using both the PA and US images and we cannot exclude that it might be easier for a neural network to replicate the reference annotations when using the same input data as the annotators that generated the labels. On the other hand, the number of learnable parameters of the networks increased with number of input channels (in this case corresponding to the number of input spectra), which may improve the performance of the networks with more learnable parameters²⁹.

Overall, our work indicates that neural network-based semantic image segmentation is feasible even with relatively small amounts of training data. Especially in combination with tools for functional parameter estimation (i.e., blood oxygenation saturation), powerful visualisations of the imaged tissue can be created.

Additional Information

The healthy human volunteer experiments were approved by the ethics committee of the medical faculty of Heidelberg University under reference number S-451/2020 and the study is registered with the German Clinical Trials Register under reference number DRKS00023205.

Acknowledgements

This project has received funding from the European Union's Horizon 2020 research and innovation programme through the ERC starting grant COMBIOSCOPY under grant agreement No. ERC-2015-StG-37960.

Bibliography

1. Jun Xia, Junjie Yao, and Lihong V Wang. Photoacoustic tomography: principles and advances. *Electromagnetic Waves (Cambridge, Mass.)*, 147:1, 2014.
2. Joanna Bruncker, Junjie Yao, Jan Laufer, and Sarah E Bohndiek. Photoacoustic imaging using genetically encoded reporters: a review. *Journal of Biomedical Optics*, 22(7):070901, 2017.
3. Paul Beard. Biomedical photoacoustic imaging. *Interface Focus*, 1(4): 602–631, 2011.
4. Benjamin T Cox, Jan Laufer, and Paul Beard. The challenges for quantitative photoacoustic imaging. In *Photons Plus Ultrasound: Imaging and Sensing 2009*, volume 7177, page 717713. International Society for Optics and Photonics, 2009.
5. Stratis Tzoumas, Antonio Nunes, Ivan Olefir, Stefan Stangl, Panagiotis Symvoulidis, Sarah Glasl, Christine Bayer, Gabriele Multhoff, and Vasilis Ntziachristos. Eigenspectra optoacoustic tomography achieves quantitative blood oxygenation imaging deep in tissues. *Nature communications*, 7:12121, 2016.
6. Yuqi Tang and Junjie Yao. 3d monte carlo simulation of light distribution in mouse brain in quantitative photoacoustic computed tomography. *Quantitative Imaging in Medicine and Surgery*, 11(3):1046, 2021.
7. Faouzi Triki and Qi Xue. Hölder stability of quantitative photoacoustic tomography based on partial data. *arXiv preprint arXiv:2103.16677*, 2021.
8. Berkan Lafci, Elena Merčep, Stefan Morscher, Xosé Luís Deán-Ben, and Daniel Razansky. Efficient segmentation of multi-modal optoacoustic

- and ultrasound images using convolutional neural networks. In *Photons Plus Ultrasound: Imaging and Sensing 2020*, volume 11240, page 112402N. International Society for Optics and Photonics, 2020.
9. Geoffrey P Luke, Kevin Hoffer-Hawlik, Austin C Van Namen, and Ruibo Shang. O-net: a convolutional neural network for quantitative photoacoustic image segmentation and oximetry. *arXiv preprint arXiv:1911.01935*, 2019.
 10. Nikolaos-Kosmas Chlis, Angelos Karlas, Nikolina-Alexia Fasoula, Michael Kallmayer, Hans-Henning Eckstein, Fabian J Theis, Vasilis Ntziachristos, and Carsten Marr. A sparse deep learning approach for automatic segmentation of human vasculature in multispectral optoacoustic tomography. *Photoacoustics*, 20:100203, 2020.
 11. Alan Yilun Yuan, Yang Gao, Liangliang Peng, Lingxiao Zhou, Jun Liu, Siwei Zhu, and Wei Song. Hybrid deep learning network for vascular segmentation in photoacoustic imaging. *Biomedical Optics Express*, 11(11):6445–6457, 2020.
 12. Serafeim Moustakidis, Murad Omar, Juan Aguirre, Pouyan Mohajerani, and Vasilis Ntziachristos. Fully automated identification of skin morphology in raster-scan optoacoustic mesoscopy using artificial intelligence. *Medical Physics*, 46(9):4046–4056, 2019.
 13. Anne Becker, Max Masthoff, Jing Claussen, Steven James Ford, Wolfgang Roll, Matthias Burg, Peter J Barth, Walter Heindel, Michael Schaefer, Michel Eisenblaetter, et al. Multispectral optoacoustic tomography of the human breast: characterisation of healthy tissue and malignant lesions using a hybrid ultrasound-optoacoustic approach. *European Radiology*, 28(2):602–609, 2018.
 14. Chen-Wei Wei, Thu-Mai Nguyen, Jinjun Xia, Bastien Arnal, Emily Y Wong, Ivan M Pelivanov, and Matthew O'Donnell. Real-time integrated photoacoustic and ultrasound (paus) imaging system to guide interventional procedures: ex vivo study. *IEEE Transactions on Ultrasonics, Ferroelectrics, and Frequency Control*, 62(2):319–328, 2015.
 15. Janek Gröhl, Melanie Schellenberg, Kris Dreher, and Lena Maier-Hein. Deep learning for biomedical photoacoustic imaging: A review. *Photoacoustics*, page 100241, 2021.
 16. Olaf Ronneberger, Philipp Fischer, and Thomas Brox. U-net: Convolutional networks for biomedical image segmentation. In *International Conference on Medical Image Computing and Computer-Assisted Intervention*, pages 234–241. Springer, 2015.
 17. Adam Paszke, Sam Gross, Francisco Massa, Adam Lerer, James Bradbury, Gregory Chanan, Trevor Killeen, Zeming Lin, Natalia Gimelshein, Luca Antiga, Alban Desmaison, Andreas Kopf, Edward Yang, Zachary DeVito, Martin Raison, Alykhan Tejani, Sasank Chilamkurthy, Benoit Steiner, Lu Fang, Junjie Bai, and Soumith Chintala. Pytorch: An imperative style, high-performance deep learning library. In H. Wallach, H. Larochelle, A. Beygelzimer, F. d'Alché-Buc, E. Fox, and R. Garnett, editors, *Advances in Neural Information Processing Systems 32*, pages 8024–8035. Curran Associates, Inc., 2019.
 18. Shruti Jadon. A survey of loss functions for semantic segmentation. In *2020 IEEE Conference on Computational Intelligence in Bioinformatics and Computational Biology (CIBCB)*, pages 1–7. IEEE, 2020.
 19. Janek Gröhl, Thomas Kirchner, Tim J Adler, Lina Hacker, Niklas Holzwarth, Adrián Hernández-Aguilera, Mildred A Herrera, Edgar Santos, Sarah E Bohndiek, and Lena Maier-Hein. Learned spectral decoloring enables photoacoustic oximetry. *Scientific Reports*, 11(1):1–12, 2021.
 20. Thomas Kirchner, Franz Sattler, Janek Gröhl, and Lena Maier-Hein. Signed real-time delay multiply and sum beamforming for multispectral photoacoustic imaging. *Journal of Imaging*, 4(10):121, 2018.
 21. Ivo Wolf, Marcus Vetter, Ingmar Wegner, Thomas Böttger, Marco Nolden, Max Schöbinger, Mark Hastenteufel, Tobias Kunert, and Hans-Peter Meinzer. The medical imaging interaction toolkit. *Medical Image Analysis*, 9(6):594–604, 2005.
 22. Steven L Jacques. Optical properties of biological tissues: a review. *Physics in Medicine & Biology*, 58(11):R37, 2013.
 23. Yun Xu and Royston Goodacre. On splitting training and validation set: A comparative study of cross-validation, bootstrap and systematic sampling for estimating the generalization performance of supervised learning. *Journal of Analysis and Testing*, 2(3):249–262, 2018.
 24. Lee R Dice. Measures of the amount of ecologic association between species. *Ecology*, 26(3):297–302, 1945.
 25. Haiying Wang and Huiru Zheng. *True Positive Rate*, pages 2302–2303. Springer New York, New York, NY, 2013. ISBN 978-1-4419-9863-7. URL https://doi.org/10.1007/978-1-4419-9863-7_255.
 26. Aleksandar Zlateski, Ronnachai Jaroensri, Prafull Sharma, and Frédo Durand. On the importance of label quality for semantic segmentation. In *Proceedings of the IEEE Conference on Computer Vision and Pattern Recognition*, pages 1479–1487, 2018.
 27. Wuwei Ren, Xosé Luís Deán-Ben, Mark-Aurel Augath, and Daniel Razansky. Feasibility study on concurrent optoacoustic tomography and magnetic resonance imaging. In *Photons Plus Ultrasound: Imaging and Sensing 2021*, volume 11642, page 116420C. International Society for Optics and Photonics, 2021.
 28. Niklas Holzwarth, Melanie Schellenberg, Janek Gröhl, Kris Dreher, Alexander Seitel, Minu D Tizabi, Beat P Müller-Stich, Lena Maier-Hein, et al. Tattoo tomography: Freehand 3d photoacoustic image reconstruction with an optical pattern. *arXiv preprint arXiv:2011.04997*, 2020.
 29. Mingxing Tan and Quoc Le. Efficientnet: Rethinking model scaling for convolutional neural networks. In *International Conference on Machine Learning*, pages 6105–6114. PMLR, 2019.

A. Annotation protocol

Appendix: Data preprocessing and annotation protocol

For data acquisition within the MS-PAB healthy volunteer study

In this protocol, we describe the means of data acquisition for the healthy volunteer study that was approved by the ethics committee of the University of Heidelberg (S-451/2020) and is registered with the DRKS (DRKS00023205).

You can find the description of the study and all relevant documents here:

https://www.drks.de/drks_web/navigate.do?navigationId=trial.HTML&TRIAL_ID=DRKS00023205

Data Preprocessing

Each of the scans will be preprocessed to fit the desired output format. This will be done in four sub-steps:

a) Cropping

Most probably, the US and PA data are not perfectly aligned directly after copying. To this end, a manual cropping step needs to be performed in order to align the images. The cropping window should be chosen with a ratio of two, e.g. 400x200 for the PA data and 200x100 for the US data (of course depending on the resolution of the reconstruction).

```
pa_data_all = pa_data_all[:, :, 79:279, WAVELENGTHS]
us_data_all = us_data_all[:, :, 35:135, :]
```

b) Averaging

To compensate for pulse laser energy fluctuations and for *slight* motion artefacts, we perform frame averaging. Since we acquire approximately 40 multispectral image stacks per recording, we subdivide the dataset into four sections of approx. ten stacks. Each of these stacks is averaged, such that we have an averaging of approx. ten frames per image stack.

```
np.mean(pa_data_all[avg_idx * pa_split_length: (avg_idx+1) * pa_split_length, :, :], axis=0)
```

c) Rescaling

In order to make the data easier to use for deep learning purposes, we rescale the image dimensions to fit 256x128 pixels. The rescaling is done with anti-aliasing in form of a Gaussian filter, which introduces another form of averaging.

```
pa_rescaled = resize(pa_data_avg, (AVERAGING_SPLITS, 256, 128, len(WAVELENGTHS)), anti_aliasing=True)
```

d) Automatic best image selection

Each of the four averaged images is subsequently automatically inspected and the image stack expressing the least blurred (the sharpest) US image is used for ground truth semantic image annotation. The sharpness is determined using the image gradients as a measure for the contrast in the image (a blurred image will not feature steep gradients, but a sharp one will):

```
gy, gx = np.gradient(array)
gnorm = np.sqrt(gx ** 2 + gy ** 2)
sharpness = np.average(gnorm)
```

Semantic Image Annotation - Labeling Protocol

The primary use case for the data is the automatic segmentation of skin (epidermis) and blood vessels in photoacoustic images. However, the transducer membrane is also easily visible in the US image and should be annotated as well. To this end, we want to label the image with the following labels:

- 1 - Artery
- 2 - Epidermis
- 3 - Other tissue
- 4- Transducer membrane
- 5 - US-Gel
- 6 - Water in US Transducer Head
- 7 - Coupling artefact
- 8 - Vein

The given numbers correspond to the values these tissue types will be assigned.

In the following, we will outline the specific instructions on how these structures are being defined based on the use of the PA and US image for creating the annotations. The goal of these definitions is to provide an unambiguous framework for deciding which class an image pixel corresponds to.

Create the segmentations

Step 1: (internal) Move your data from the data/ folder to the data_labels/ folder.

Step 2: Load the data *_us and *_pa into the MITK workbench

Step 3: Open the multilabel segmentation plugin

Step 4: Select the patient image to be the photoacoustic image

Step 5: Create a new segmentation session and accept the name. Press cancel on naming the segmentation.

Step 6: Right-click on the labels in the data manager

Step 7: Click load preset

Step 8: In order to facilitate creating the label instances, you should use the provided *labelset-extended.lsetp* file.

Step 9: Maximise the red window and move the Axial slider to 0. Move the US image to the top and that's it.

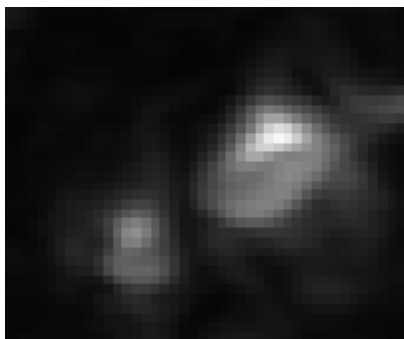
Step 10: Segment away!

1 - Blood Vessel

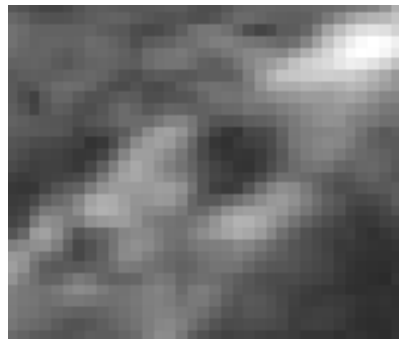
Blood vessels have a number of criteria that define them in the PA and US images:

- **PA signal is higher** than the background tissue
- **US signal is lower** than the background tissue
- Characteristic **spectrum** for arteries and veins
- A vessel must enclose at least three pixels in x and z-direction.
- The final shape of the image will be determined by both the PA and US signal. However, when in doubt, the PA signal wins.

Decisive for the final segmentation is the **signal in the PA image**. This means that the PA signal area needs to be annotated, even if the ultrasound image would itself not warrant annotation.



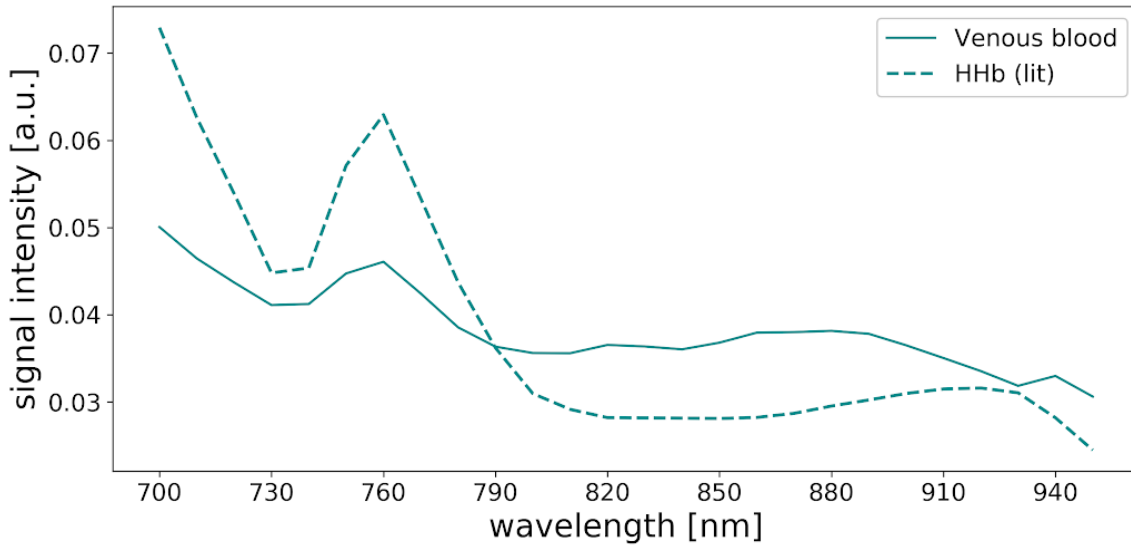
PA Image of vessels



Corresponding US Image

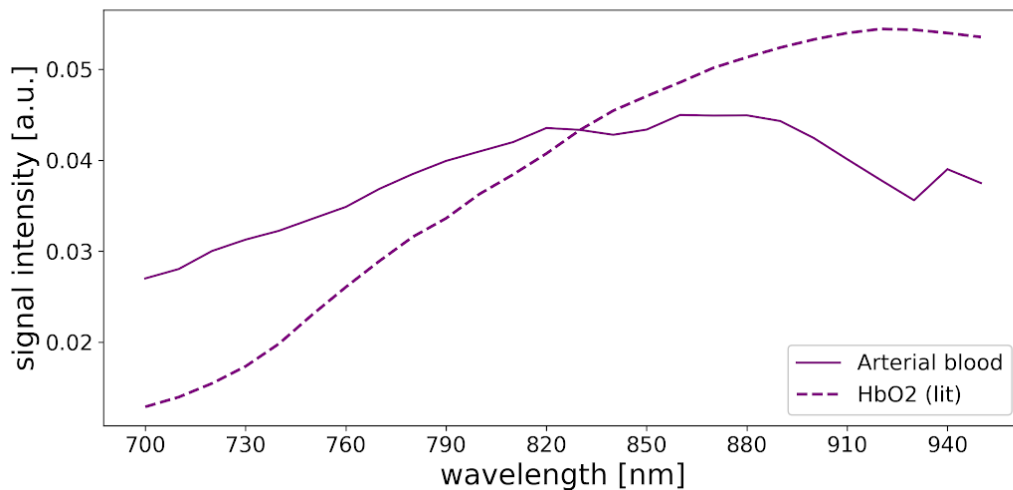
Vein spectrum:

First, there is a decrease in signal intensity, then an increase again for a short peak followed by a decrease of the signal.



Artery spectrum:

There is a steady increase of the spectrum over the wavelength range. Above 850nm signal decreases because of the influence of water and the influence of the laser pulse energy.



2 - Epidermis

The epidermis is the outermost layer of the skin. It can be defined with the following criteria:

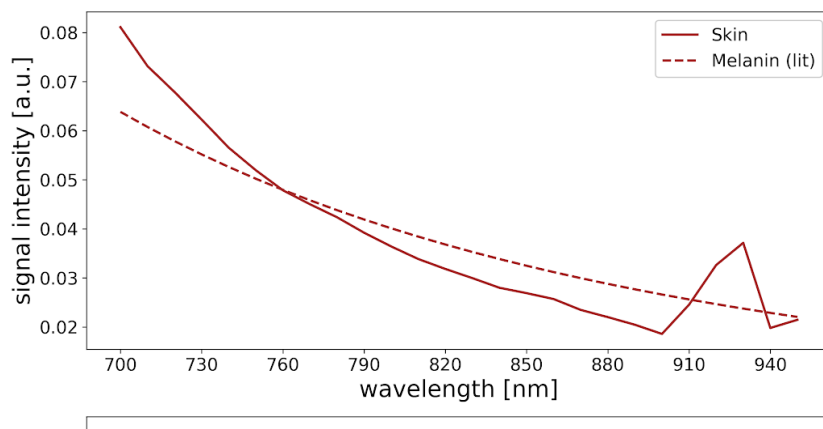
- A characteristic **spectrum** that shows a steady decrease of the signal over the wavelengths
- Usually stretches over the **entire image slice**
- **PA signal is high** especially in the 700-800nm range

- **US signal is high** compared to other tissue
 - Try to aim for 2-4 pixels in depth. When in doubt, make it thinner.
- Decisive for the final segmentation is the **signal in the US image**.



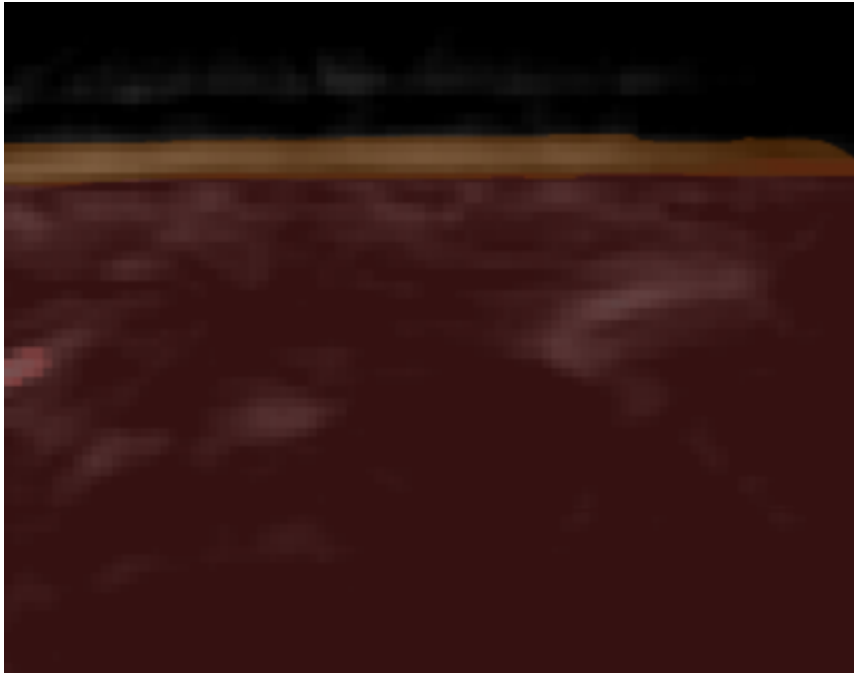
Example photoacoustic image of the skin.

Epidermis spectrum:



3 - Other Tissue

After defining the vessel structures and the epidermis, all remaining pixels from the epidermis **down** to the end of the image will be classified as “other tissue”.



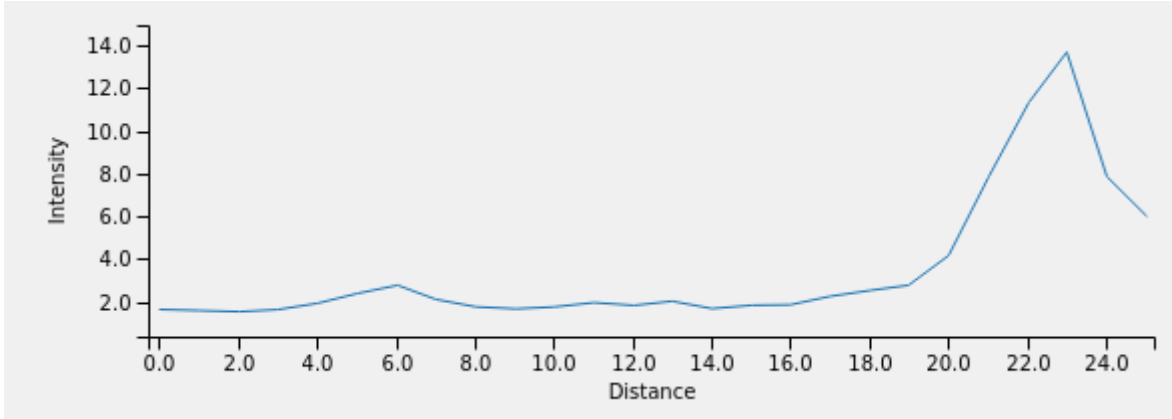
Example segmentation of background tissue, here shown in red. The brown-labelled epidermis indicates the border of the “other tissue” area.

4 - Transducer Membrane

The transducer membrane can be identified by the following features:

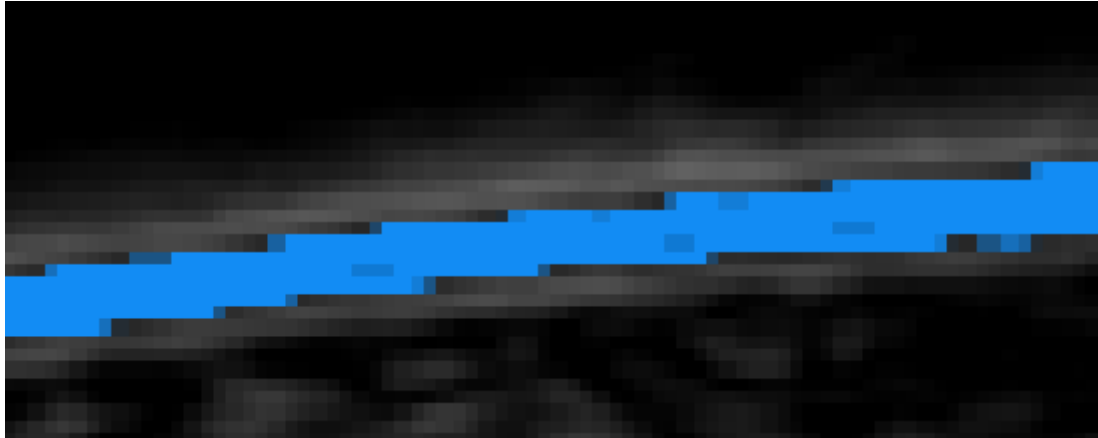
- Virtually **no PA signal** except for the 900-950nm range
- **High US signal** with great contrast compared to the water above and the US gel below.
- Similar shape to the epidermis layer, as it adjusts to its shape
- Try to aim for 3-5 pixels in size

Decisive for the final segmentation is the **signal in the US image**.



5 - US-Gel

Defined as the area **between** the **epidermis** segmentation and the **transducer membrane** segmentation. It usually shows as not having a distinct spectrum and barely any signal in the PA and the US image. Segmentation of the US gel layer might be crucial, as different operators might apply different amounts of ultrasound gel resulting in significant differences in layer size.



The US-Gel layer is in-painted in blue in this example.

6 - Water in US Transducer Head

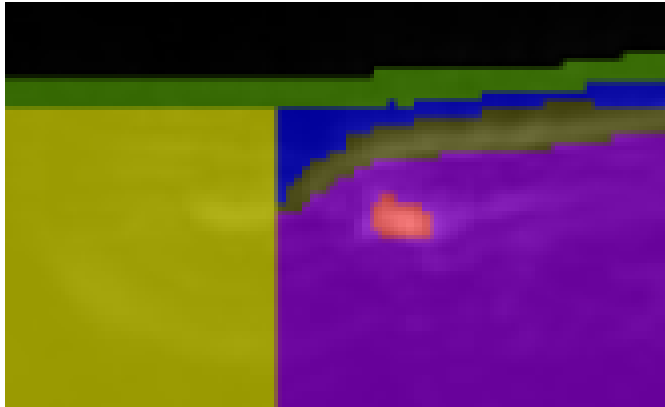
The water area is defined in a similar manner to the “other tissue” segmentation class. Its lower border is the segmentation of the transducer membrane and it extends all the way up to the top of the image.

7 - Coupling Artefact

In some cases, the transducer head might not be placed perfectly on top of the skin, leaving an area where the probe does not have contact, thus resulting in an area without US contribution. The coupling artefact can be identified by the following criteria:

- **Lack of signal** in the PA image
- **Lack of signal** in the US image
- Except for the beginning after the membrane, where there is a **total reflection** of the incoming signal happening at the air interface.

The boundary of this class is defined to be a **straight** line from the last signal of the skin that is still measurable. Towards the top, the area is limited by the transducer membrane. Decisive for the final segmentation is the signal in the **US and PA** image.

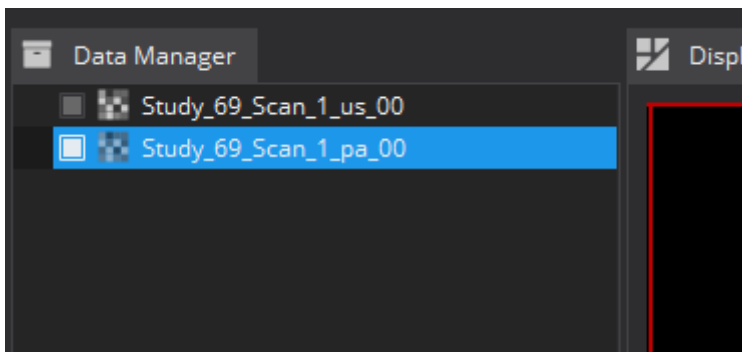


In this example, the PA image is annotated. Red is a blood vessel, purple denotes generic tissue, brown is the skin, and green is the transducer membrane. One can clearly see the missing signal in the area without coupling (yellow).

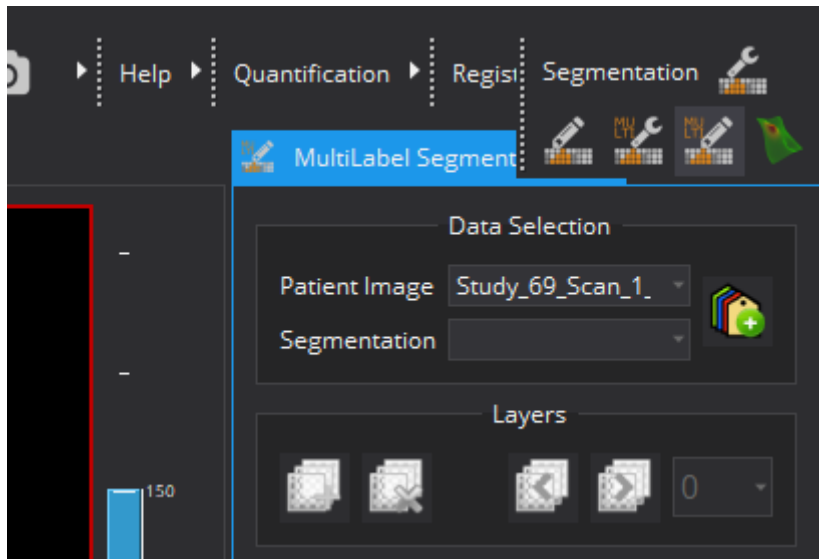
Imaging example using MITK

MITK can be installed at www.mitk.org

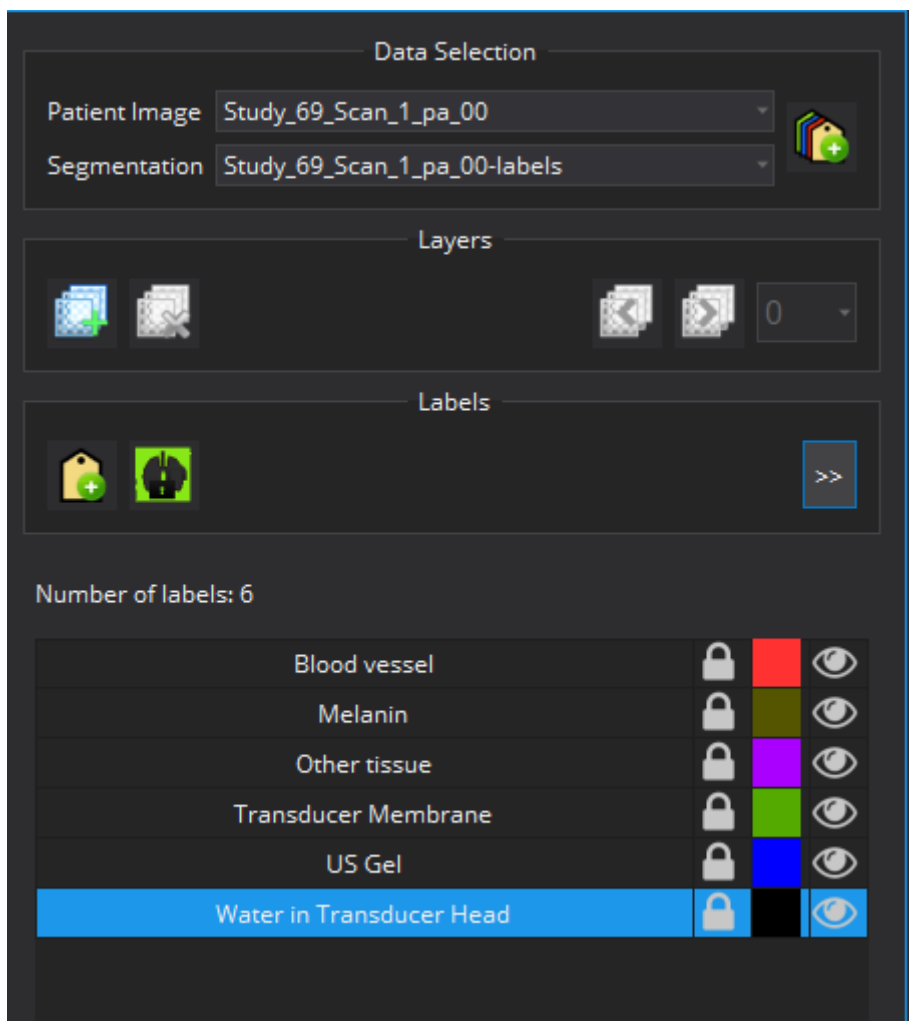
1. Load PA and US images



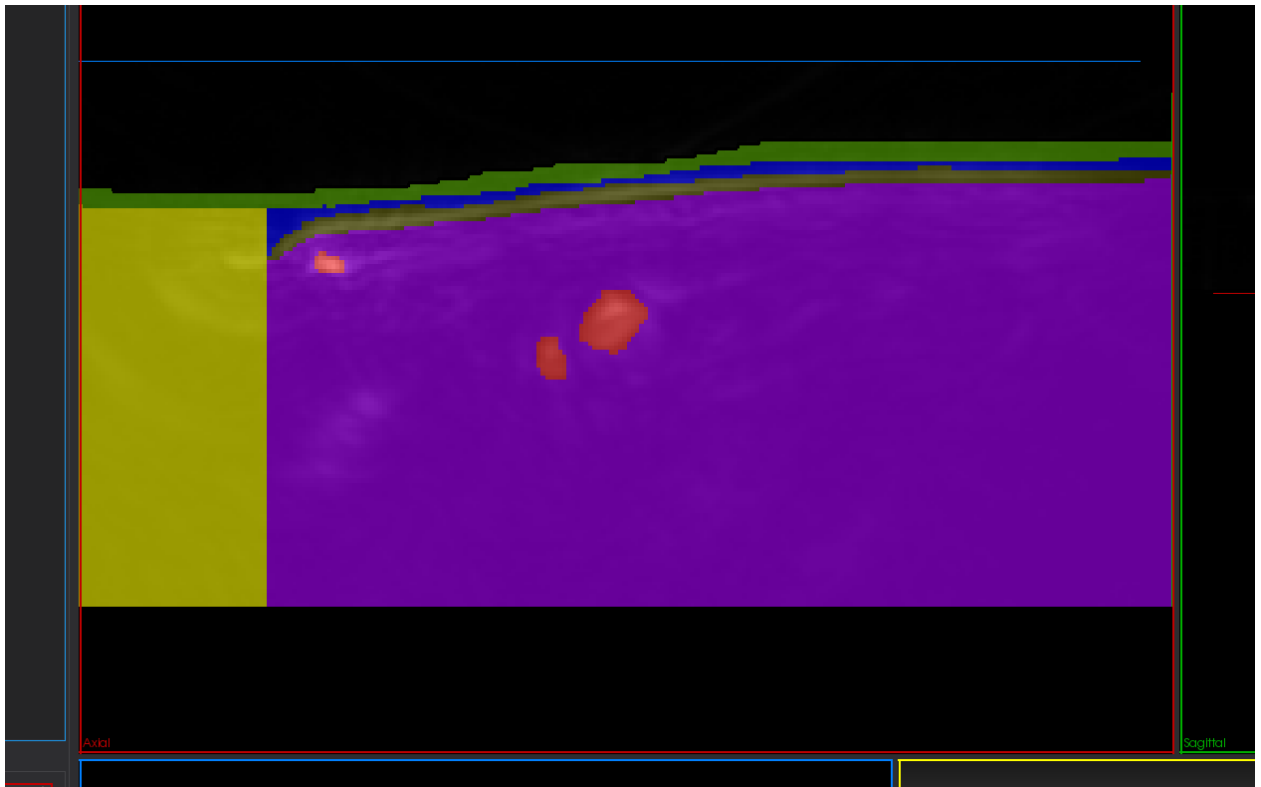
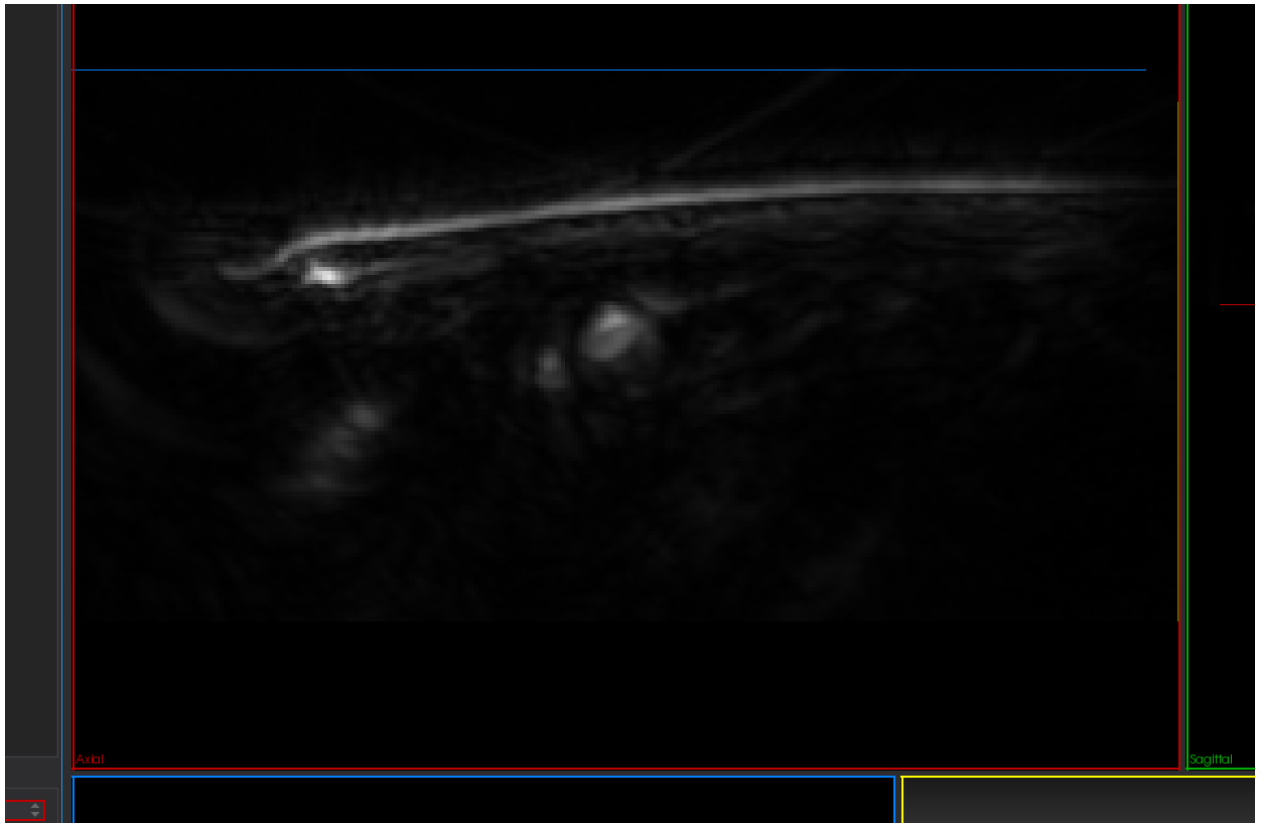
2. Open MultiLabel Segmentation Tool



And create the segmentation labels



3. Do annotations



4. Saving the results

Right-click on the annotation object and “Save...”

